J. Fluid Mech. (2008), *vol.* 614, *pp.* 329–354. © 2008 Cambridge University Press
doi:10.1017/S0022112008003522 Printed in the United Kingdom

Multi-branching three-dimensional flow with substantial changes in vessel shapes

R. I. BOWLES, N. C. OVENDEN AND F. T. SMITH

Department of Mathematics, UCL, Gower Street, London, WC1E 6BT, UK

(Received 15 August 2007 and in revised from 23 June 2008)

This theoretical investigation of steady fluid flow through a rigid three-dimensional branching geometry is motivated by applications to haemodynamics in the brain especially, while the flow through a tube with a blockage or through a collapsed tube provides another motivation with a biomedical background. Three-dimensional motion without symmetry is addressed through one mother vessel to two or several daughters. A comparatively long axial length scale of the geometry leads to a longitudinal vortex system providing a slender-flow model for the complete mother-and-daughters flow response. Computational studies and subsequent analysis, along with comparisons, are presented. The relative flow rate varies in terms of an effective Reynolds number dependence, allowing a wide range of flow rates to be examined theoretically; also any rigid cross-sectional shape and ratio of cross-sectional area expansion or contraction from the mother vessel to the daughters can be accommodated in principle in both the computations and the analysis. Swirl production with substantial crossflows is found. The analysis shows that close to any carina (the ridge separating daughter vessels) or carinas at a branch junction either forward or reversed motion can be observed locally at the saddle point even though the bulk of the motion is driven forward into the daughters. The local forward or reversed motion is controlled, however, by global properties of the geometry and incident conditions, a feature which applies to any of the flow rates examined.

1. Introduction

The interest in three-dimensional internal fluid flow with branching is motivated primarily by haemodynamics in the brain (Kufahl & Clark 1985; Hillen, Hoogstraten & Post 1986; Zagzoule & Mark-Vergnes 1986; Hillen *et al.* 1988; Hademenos, Massoud & Vinuela 1996; Gao *et al.* 1997; Ursino & Lodi 1997; Olufsen 1999; Cassot, Zagzoule & Marc-Vergnes 2000; Ferrandez *et al.* 2000) although it is also relevant to much of the human system, including the cardiovascular tree, the lungs, the lower urinary tract. Applications within the brain include arteriovenous malformations, the Circle of Willis, the whole cerebral network or its sub-networks, as well as the carotid arteries. The study has to be spatially three-dimensional by virtue of the cerebral geometry itself and the complicated three-dimensional fluid flows within the vessels of the brain. This fully three-dimensional nature implies that substantially new problems will be encountered and that two-dimensional or axisymmetric approaches, as used in most previous theories, become invalid.

The three-dimensional changes of internal wall shape involved in the branchings listed above also arise in realistic modelling of blockage effects in tubes, such as in the ureter or urethra in the urinary tract (Griffiths 1971, 1987; Griffiths *et al.* 1987;

https://doi.org/10.1017/S0022112008003522 Published online by Cambridge University Press

Cummings, Wattis & Graham 2004). The flow through collapsed tubes (Luo & Pedley 2000; Marzo, Luo & Bertram 2005) provides another application and motivation, derived from a biomedical background. The three-dimensional shapes occurring in collapsed tubes as sketched in Grotberg & Jensen's (2004) figure 2 for example, with contact of opposite tube walls, are very similar in their geometry to those of many three-dimensional branchings; this last paper also notes in passing Bertram & Godbole's (1997) visualizations of the steady three-dimensional motion downstream which shows twin jets with flow reversal between them.

A great deal of theoretical, analytical and numerical work, and a experimental work, has been done on two-dimensional models. Some work in three dimensions exists (Smith 1977; Bennett 1987; Pedley 1997; Blyth & Mestel 1999; Smith & Jones 2000) but tends to assume some form of symmetry, such as in the incoming mother vessel shape and in the ensuing daughter vessel shapes.

In contrast, a fairly general three-dimensional rigid branching from one mother vessel to a number of daughter vessels is considered in the present study. We make no assumption of symmetry and the mother vessel has upstream shaping of its walls in anticipation of a bifurcation or multiple branching at a branch junction. See the diagrams in figure 1 (*a–c*). An important aspect, whether for the local branch junction or more globally within a network of vessels, is the influence of this shaping on the flow ahead of any branching. This is studied by Smith *et al.* (2003*b*) and others for two-dimensional flows and it is found that wall shaping can have a significant direct impact on the incident motion. Upstream shaping within the mother vessel can be seen in various forms in Zhao & Lieber (1994), Wilquem & Degrez (1997), Tadjfar & Himeno (2001) and elsewhere but seems to be largely ignored in theoretical investigations apart from studies by Comer, Kleinstreuer & Zhang (2001*a*, *b*), Smith & Jones (2000) and Smith *et al.* (2003*b*). The biomedical applications of multiple branching, in particular with regard to arteriovenous malformations, are described in a number of the references in this last paper. The present investigation includes these relevant, largely unstudied, non-symmetrical three-dimensional effects of three-dimensional wall shaping, presuming them to act over a relatively long axial length scale. Such an assumption seems reasonably valid in many parts of the cerebrovascular system, owing simply to the slender physical shapes of the vessels involved, while concerning other shapes the results of Tadjfar & Smith (2004) indicate the possible validity of the approximations made subsequently in this paper for significantly non-slender shapes such as with a right-angled bend, suggesting a very wide range of applicability in practice. As a result, the geometry and hence the flow adjusts a great deal before the ridge separating neighbouring daughter vessels, from here onwards knows as the carina, is reached. This slender approach, while being computationally efficient, is also able to handle substantial changes in cross-section and we aim to explain the appearance of forward and reversed flows near the carina together with their three-dimensional background. Here Comer *et al.*'s (2001*a*) direct simulation results which are for bifurcations over a small number of generations are relevant. (Their paper also mentions some supporting experimental results for a single bifurcation.) Their results indicate, among other interesting phenomena, axial flow separation occurring in some cases, especially at higher flow rates, and the current analysis aims to capture and explain such observed phenomena.

For any individual branching within a network there is of course a global upstream or feedback effect because of the presence of overall pressure differences which act across the larger network present. These pressures and global network properties influence the incident mass flux ahead of a particular branching. We take that mass

https://doi.org/10.1017/S0022112008003522 Published online by Cambridge University Press

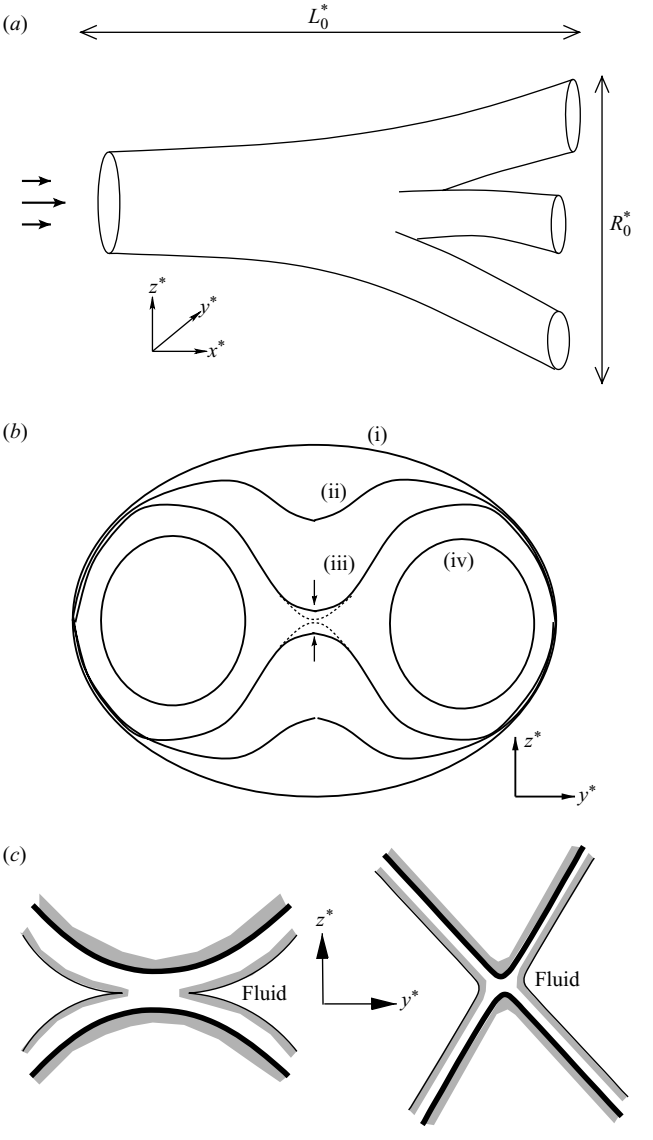


FIGURE 1. (*a*) The three-dimensional multi-branching geometry with a relatively long axial scale in the mother and daughters. (*b*) Representative cross-sectional shapes in the (y, z)-plane approaching the carina's saddle point, and the axial evolution of typical cross-sectional shape (shown (i)–(iv)). (*c*) Representative cross-sectional shapes in the (y, z)-plane just before (thick curves) and just after (thin) a carina: left, flat cusp-forming pinch; right, marginal corner-forming pinch.

flux as given in this study, and focus on the more local upstream effects that come into operation. Such effects have two main causes: the upstream shaping of the wall in the mother, mentioned above, and the inherent upstream influence in the fluid flow itself. Here we concentrate on the upstream shaping, given that alterations in the three-dimensional cross-sectional shape in the mother prior to the carina and to the beginning of the daughters can control much of the flow adjustment in readiness for entry into the daughters. The inherent upstream influence from the branching then

https://doi.org/10.1017/S0022112008003522 Published online by Cambridge University Press

enters spatially later in the process over a relatively shorter scale much closer to the carina, a matter we discuss in more detail in § 2, below.

The local closure of the mother vessel at a typical carina clearly is very much a three-dimensional property and two-dimensional models have no corresponding feature. The carina can be generated in several different ways by the cross-sectional alterations present such as (i) in a pinch form leading to cusps immediately downstream of the carina or (ii) in a marginal form, leading to an effective corner immediately downstream as shown in figure 1(*c*). The local flow behaviour near the carina may be of inherent importance in circumstances involving, for example, particle deposition (see Comer *et al.* 2001*a*, *b*), drug delivery or glue positioning in the context of endovascular treatment of arteriovenous and other vascular malformations (Handa *et al.* 1993; Stacey & Kitchen 1999; Gnanalingham, Taylor & Watkin 2002). The current theoretical study therefore may provide some guidance not only in the placement of a catheter delivering this glue ahead of a carina but additionally to strategies used in alternative therapies such as surgical clipping of abnormal branching vessels. Similar considerations apply in the context of collapsed tubes.

This paper describes a theoretical examination of incompressible steady laminar three-dimensional steady flow within a rigid three-dimensional internal branching geometry. Section 2 describes the model system under discussion in which a relatively long axial length scale is supposed, leading to a parabolic set of equations which describe a longitudinal vortex-like problem for the branching three-dimensional motion. The comparative flow rate varies in terms of an effective Reynolds number dependence, and any ratio of cross-sectional area expansion or contraction from the mother vessel to the daughters can be accommodated. Numerical solutions are addressed in § 3. Each case, to repeat, is set at a given fixed in-flow mass flux rather than with specified end pressure differences applied to the branched configuration. Swirl production with substantial crossflows is observed clearly in the results. Sections 4 and 5 derive certain analytical properties holding close to the saddle point of the carina and compare these with the numerical findings. Further comments are then presented in § 6.

2. Length scales and the model problem

The three-dimensional geometry shown in figure 1(*a–c*) is taken to have a dimensional axial length scale L_0^* which is much larger than the cross-sectional length scale based on the typical vessel radius R_0^*. Defining a geometrical aspect ratio $\alpha = R_0^*/L_0^* \ll 1$, typical angles of divergence of the daughter branches are assumed small and of order α. The dimensional Cartesian coordinates x^*, y^*, z^* are used, with x^* being the axial coordinate (see figure 1*b*). The corresponding dimensional velocity components are then defined as u^*, v^*, w^* with the dimensional pressure represented as p^*. The Reynolds number Re is based on the longer axial length scale and is given by

$$Re = U_0^* L_0^* \rho_0^* / \mu_0^* \tag{2.1}$$

where U_0^* is a representative dimensional axial in-flow velocity and ρ_0^* and μ_0^* are the fluid density and viscosity respectively. The variables are non-dimensionalized as follows:

$$[x^*, y^*, z^*] = [L_0^* X, R_0^* y, R_0^* z], \quad [u^*, v^*, w^*] = [U_0^* u, U_0^* \alpha V, U_0^* \alpha W] \tag{2.2}$$

https://doi.org/10.1017/S0022112008003522 Published online by Cambridge University Press

and $p^* = \rho_0^* U_0^{*2}(\pi_1(X) + \alpha^2 \pi_2(X, y, z))$. These scalings on velocity are implied by the continuity balance while those involved in the pressure response stem from the axial momentum balance as far as the $O(1)$ term, independent of y and z, is concerned and from the cross-sectional momentum equations for the $O(\alpha^2)$ contribution which depends on y, z as well as X. Hence the full continuity equation for $\boldsymbol{u} = (u, V, W)$,

$$\nabla \cdot \boldsymbol{u} = 0 \tag{2.3a}$$

is obtained, along with the X-momentum equation

$$(\boldsymbol{u} \cdot \nabla)u = -\pi_1'(X) + \Gamma \Delta u \tag{2.3b}$$

and the cross-sectional momentum balances

$$(\boldsymbol{u} \cdot \nabla)V = -\partial \pi_2 / \partial y + \Gamma \Delta V, \tag{2.3c}$$

$$(\boldsymbol{u} \cdot \nabla)W = -\partial \pi_2 / \partial z + \Gamma \Delta W. \tag{2.3d}$$

Here the parameter $\Gamma = 1/(\alpha^2 Re)$ and ∇ is the gradient vector operator $(\partial_X, \partial_y, \partial_z)$. Also Δ is the two-dimensional Laplacian operator $(\partial_y^2 + \partial_z^2)$ since longitudinal diffusion is negligible over the current axial length scales. So for a given slender geometry, with given length scale α^{-1}, the flow response depends on the flow rate through the value of Γ (which reflects the influence of Re). The governing equations to solve are the long-scale ones (2.3*a–d*) together with incident boundary conditions upstream in the mother and no-slip conditions at all the walls inside the mother and the daughters, essentially as in Tadjfar & Smith (2004). In general, there is nonlinear inertial–viscous balancing of the flow in the mother vessel and daughter vessels as described by (2.3*a–d*). Viscous filling of the flow in the vessels also takes place, referring to the sublayers which, although relatively thin at the upstream end, grow in thickness as the downstream distance increases and then tend towards merger as their thicknesses become comparable with the typical tube width. Constrictions, dilations, blockages, wall roughnesses and so on, whether symmetrical or not, can also be accommodated within this approach.

Concerning the upstream influence, inherent in the flow, from a branching, blockage or other distortion of length scale $x \sim 1$, the maximum upstream influence length is only of order $\ln(Re)$ from Smith (1978). This upstream-influence length scale is negligible therefore compared with the length scale α^{-1} associated with (2.3*a–d*) in most realistic circumstances. This is the case whether the flow is axisymmetric or otherwise and even if nonlinear effects on the shorter length scale are present, such as $O(1)$ divergence angles of the daughters. Further, the Tadjfar & Smith (2004) numerical findings and comparisons imply that small-angle theory appears to work well even for $O(1)$ divergence angles, thus perhaps tending to reduce the significance of upstream influence. We restrict our attention therefore to the parabolic system (2.3*a–d*).

Three regimes of interest (*a*)–(*c*) can now be identified.

(*a*) If the flow rate is comparatively low such that $Re \ll \alpha^{-2}$ then the parameter Γ is large and we have effectively zero inertia according to (2.3*a–d*) with π_1, π_2 each scaled with respect to Γ. In consequence viscous and pressure effects, i.e. three-dimensional lubrication-like effects, dominate in this regime. The flow rate here represented by Re can be low, medium or large, with the low-flow-rate case tending to be associated more with motion inside capillaries in the physiological context. Alternatively for a given Re the non-dimensional lengths involved here have to exceed the order of Re. This is clearly already implied by the regime we are considering here but the

https://doi.org/10.1017/S0022112008003522 Published online by Cambridge University Press

point is made in terms of a fixed Reynolds number rather than axial length. Also the non-dimensional length must be large as well as being in excess of Re. The linear reduced three-dimensional lubrication-like system inferred for the present regime in fact can hold throughout for the multiple carinas and branchings, thus including the entire geometry, as demonstrated later.

(b) If $Re \sim \alpha^{-2}$, so that Re must be large, then the value of Γ is of $O(1)$ and the full longitudinal-vortex system (2.3a–d) above applies. This response is viscous–inviscid, nonlinear and usually requires computation: see below.

(c) If $Re \gg \alpha^{-2}$, corresponding again to a large effective flow rate Re, then formally the inertial and pressure terms alone act to leading order in (2.3a–d) since Γ is small and so the implied behaviour is three-dimensional inviscid. This regime of comparatively high flow rates will be taken up again later. The ordering in this regime is $1 \ll \alpha^{-2} \ll Re$.

All the cases (a)–(c) however are in effect covered by regime (b) and hence our focus will be mostly on that regime. The inviscid system in regime (c) could of course be addressed but the inherent viscous wall layers there would also need tackling in detail, which suggests that the viscous–inviscid system of (b) is better addressed first followed by analysis of the effects of reduced viscosity: again this is demonstrated later. Reasoning similar to that leading to cases (a)–(c) applies if Re is large and fixed instead and various length scales are then considered but the biomedical setting seems best developed as a model in terms of the relative length scale α^{-1} being large.

3. Computational study

The relatively long-scale governing system (2.3a) to (2.3d) is parabolic and there is no upstream influence at all apart from the direct cross-sectional shape changes as long as the axial velocity component u remains positive, corresponding to forward flow. The numerical approach below marches forward axially through the mother vessel to a branch junction and on into the daughter vessels. Appropriate boundary conditions are no slip at the mother or daughter tube walls in $X > X_{-\infty}$ say and a given starting condition on the velocity components at $X = X_{-\infty}$, corresponding to fully developed parallel flow, so fixing the total mass flux. A gradual 'dumbbell' effect comes into the cross-section shapes, station by station, as if in a pinch process – see figure 1(b). This change in the wall position is accommodated by modifying the Cartesian gridding method described in Smith *et al.* (2003a) and Tadjfar & Smith (2004) and allows for quite general tube shapes at each axial station, essentially by transferring the wall conditions to the nearest grid point. A validation of this method in numerical terms is given in the two papers just mentioned, which also make a comparison of similar three-dimensional flow solutions with direct simulation of the Navier–Stokes equations. There are firm links with the immersed-boundary method described by Peskin (2002) and Mittal & Iaccarino (2005). Analytical transformations are used to let the grid centre vary with X and the outer boundary of the grid expand or contract, wherever necessary, as X increases.

Incoming velocity profiles that are either uniform or satisfy the no-slip constraint at the walls can be accommodated at $X_{-\infty}$ where the main pressure π_1 is set to zero, without loss of generality. The velocity and pressure solution at the next X station is then obtained iteratively by means of semi-implicit differencing with uniform grid sizes in X, y, z. First π_1 is guessed and the other velocity components V and W are initially set to known values at the preceding axial station; then (2.3b) is solved in difference form for u in the whole interior; the total mass flux thus produced in

https://doi.org/10.1017/S0022112008003522 Published online by Cambridge University Press

difference form, integrated over the cross-section, is compared with the prescribed flux value; and π_1 is adjusted to make the two fluxes equal. The wall boundary conditions on u are accommodated within this iteration procedure. Second, (2.3a, c, d) are treated in a secondary-vorticity – velocity formulation, coupled through iteration, with differencing and successive solution throughout the interior of the grid being performed in a fashion similar to that for (2.3b). The boundary conditions on vorticity are derived from the latest updated values of secondary wall shear whereas those on V and W follow directly from the no-slip requirement. The iterations here are continued until a convergence criterion is met on the maximum absolute differences between successive iterates as in the papers by Smith *et al.* (2003a) and Tadjfar & Smith (2004) above. The procedure is repeated at each subsequent X station in a marching manner. The approach is second-order accurate in the cross-section, apart from the wall-fitting effect, and it is made second-order accurate in the axial direction by means of the double-stepping procedure described in Smith & Timoshin (1996). The typical grids used have 101 by 101 or 201 by 201 points in the cross-section and an axial step length of 0.000001 (see also comments on the grid effects below), although this does vary from case to case.

The results are presented in figures 2–7, showing the computed flows marching through the mother tube to the carina and branching, and on into the daughter tubes for various cases. The upstream starting station $X_{-\infty}$ is taken as zero without loss of generality. The model wall shapes for all cases are of algebraic form, having an 'upper' z value dependent on X, y given by

$$z_{\rm upper}(X,y) = b_h(X)\left[1-\left(\frac{y}{a_h(X)}\right)^2\right]^{1/2} - \sum_{m=1}^{M} H_m(X)G_m(y-y_m(X)) \qquad (3.1)$$

along with a lower one $z_{\rm lower}$ given by $-z_{\rm upper}$. Here $H_1(X) = h_1 F(X)$ with the constant h_1 being specified for each case, while the functions $H_2(X)$, $H_3(X)$ and so on vary from case to case as does the number M of carinas or number $M+1$ of daughter vessels. In the current examples we take $H_{2,3}(X) = h_{2,3}F(X)$ and choose values for $h_{2,3}$. The function $F(X)$ is $(X/X_2)^2$ for $X < X_2$ but $(2X - X_2)/X_2$ for $X > X_2$ where X_2 is a specified station downstream of $X_{-\infty}$, taken to be unity. Also $[a_h(X), b_h(X)] = [a_1, b_1](1-rF(X))$ with the constants r, a_1, b_1 chosen to be -1.2, 1 and 1 respectively in the present calculations. A shift in the centreline of the vessels is also incorporated in (3.1) although in the present studies we work with a zero shift. For figures 2, 3 and 5, 6, we take $G_m(s) = (1+8s^2)^{-1}$ and for figure 4, $G_m(s) = \exp(-8s^2)$ and we take $y_1 = 0$, $y_2 = a_h/2$, $y_3 = -a_h/2$. The parameters are adjusted to alter the branching geometry in the results which follow, the geometry being shown in each figure together with particular parameters.

Figure 2(a–c) shows one mother vessel and two daughters, so that in (3.1) the number M is unity or in effect $H_2(X)$, $H_3(X)$ and so on are all zero. The pinching of the mother cross-section on approach to the carina is seen in figure 2(a) and the general geometrical trend of the shape is clearly a constricting one and it is not surprising to find that the resulting flow is wholly forward. figure 2(b) illustrates this with plots of the axial velocity component $u_{\rm cl}$ along the centreline ($y = z = 0$) and the major pressure component π_1 against the scaled axial distance X. This case has $\Gamma = 1$ with the carina positioned at the station $X = X_c \approx 0.79$, in line with the cutoff of $u_{\rm cl}$ there, while we observe for later use that π_1 appears to behave smoothly at that station. In figure 2(c) the axial velocity profiles $u = u_{\rm mid}$ evaluated at zero z are presented at increasing X stations along the branching system and the parabolic

https://doi.org/10.1017/S0022112008003522 Published online by Cambridge University Press

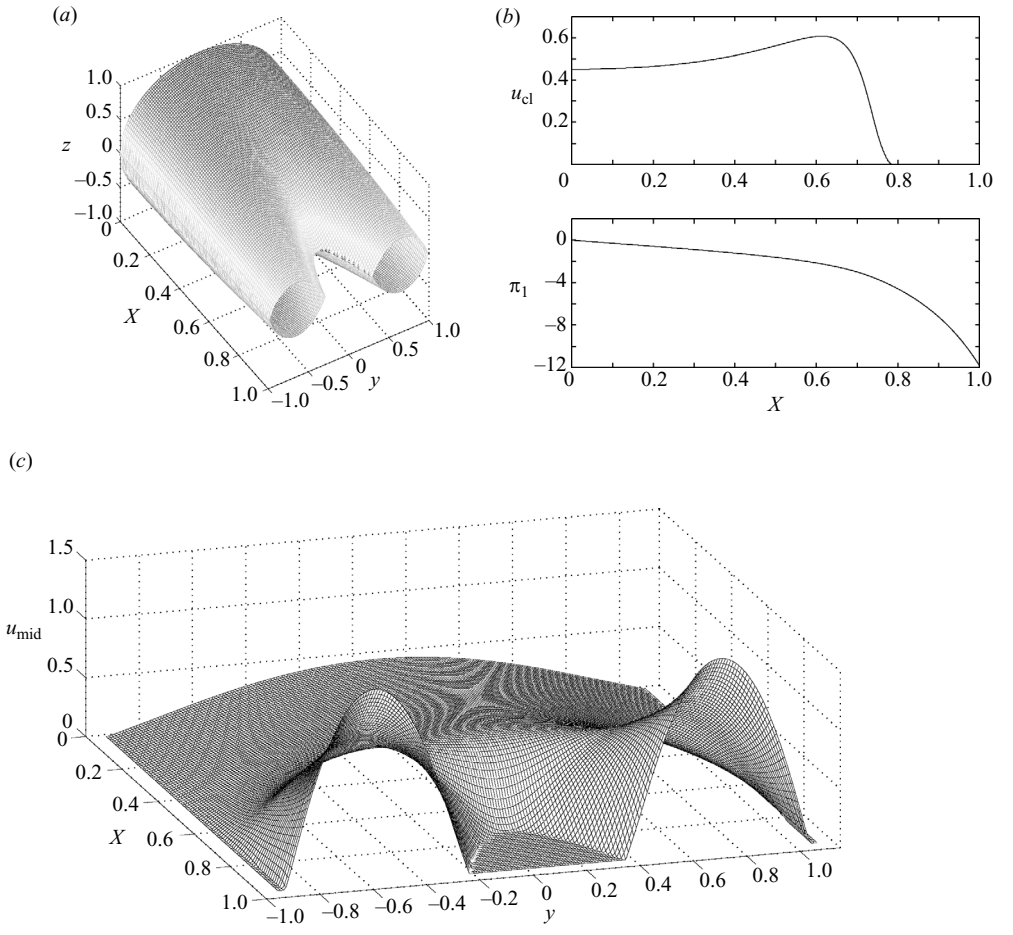


FIGURE 2. Results for one mother splitting into two daughters with a constriction in overall cross-sectional area. Here, $\Gamma = 1$, $h_1 = 1.6$. (*a*) Branching geometry. (*b*) Plots of u_{cl}, π_1 against X. The saddle point of the carina occurs at $X = 0.79$. (*c*) Surface plot of the axial velocity u in the plane $z = 0$.

velocity profiles at inflow and outflow are clear. In the mother vessel u_{mid} appears to plummet locally to zero as the saddle of the carina is approached and indeed the theory in the next section implies that u_{mid} should behave like y^4 locally, a behaviour which seems consistent with the results here, as shown in figure 2(*c*). In the daughters the fluid accelerates due to the constricting effects.

Figure 3(*a–c*) is for three daughters and hence two carinas ($M = 2$) and in addition the vessel shapes are now generally expanding in the axial direction, as is shown in figure 3(*a*). In this case Γ is 1/100. Figure 3(*b*) plots the calculated mother-centreline velocity u_{cl} and pressure π_1 versus X; generally the local response near the first carina is similar to that above. Likewise figure 3(*c*), which gives the axial velocity profiles u_{mid} at various X stations, shows in the mother vessel the velocity u_{mid} plunging to zero locally as the saddle point of the first carina is approached. In the three daughters, however, the fluid now decelerates owing to the vessel expansion effects and we see the occurrence of negative u values at some locations, corresponding to flow reversal. This feature of the flow is illustrated for a different case in figure 4

https://doi.org/10.1017/S0022112008003522 Published online by Cambridge University Press

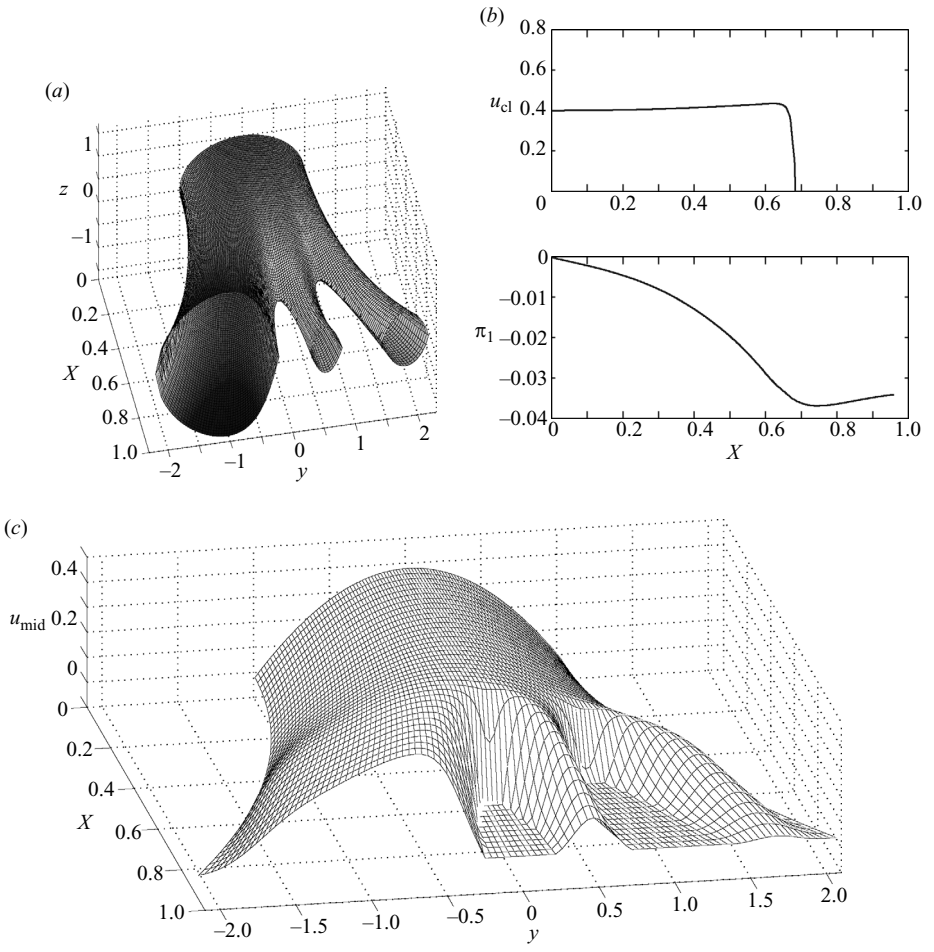


FIGURE 3. Results for three daughters with the vessels expanding axially. Here $\Gamma = 1/100$, $h_1 = h_2 = 2.8$. (*a*) Branching geometry. (*b*) Plots of u_{cl} and π_1 vs X. (*c*) Surface plot of axial velocity profiles u_{mid} in the symmetry plane $z = 0$.

below. Strictly the π_1 values should be different in each daughter here but the suggested trends are confirmed in the subsequent results.

A relatively rapid change in the cross-sections of the vessels accompanied by a relatively large flow rate is addressed in figure 4(*a–c*) which is for three daughters and two carinas and has $\Gamma = 1/1000$. In this case the axial velocity profiles u_{mid} as displayed in figure 4(*b*) at successive axial stations show that in the mother the axial velocity soon passes through zero and the flow reverses substantially even before the saddle point of the carina is encountered. The flow reversal is because of the combination of a higher flow rate, an expanding cross-sectional vessel shape and the axial pressure gradient being slightly adverse at the first reversal station.This flow reversal is further illustrated in a plot of wall shear in figure 4(*c*). Note that the numerical approximation to the wall shape is close but is nevertheless non-smooth. This means in particular that there is an effective thin sublayer close to the approximate non-smooth wall that is used numerically, in which the main distortions from the true-wall flow occur. The rather enhanced influence of the approximation on

https://doi.org/10.1017/S0022112008003522 Published online by Cambridge University Press

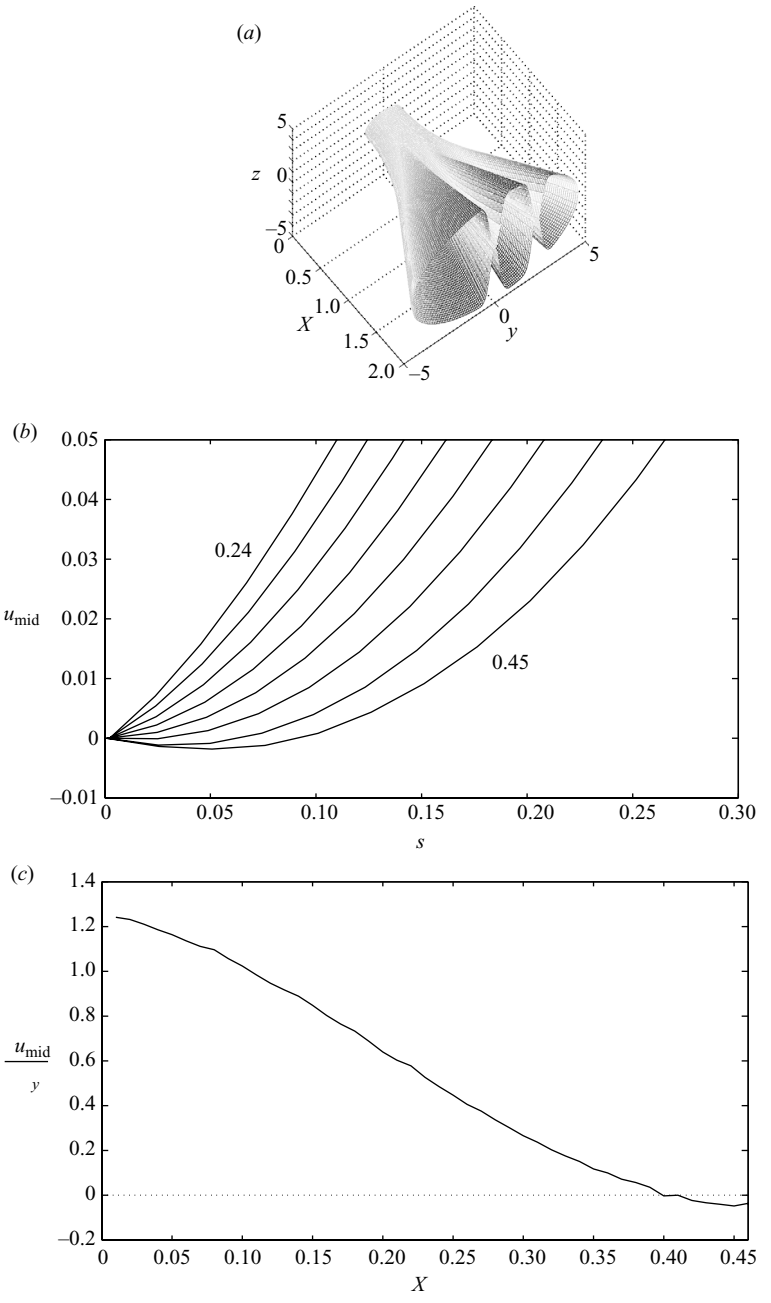


FIGURE 4. Results for one mother splitting into three daughters, with relatively large rapid increase in overall cross-sectional area in the vessels. Here, $\Gamma = 1/1000$, $h_1 = 1.6$. (*a*) Branching geometry. (*b*) Local profiles u_{mid} at various X stations ($X = 0.24$, 0.27, 0.30, 0.33, 0.36, 0.39, 0.42, 0.45), showing the development of flow reversal at the outer wall. Here s measures the distance from the wall, measured into the fluid. (*c*) Plot of $\partial u_{\mathrm{mid}}/\partial y$ at the outer wall against X.

the wall shear compared with the influence on other significant properties is therefore not surprising. By contrast, the cases studied by Tadjfar & Smith (2004) are for walls which have uniform cross-section, except at a junction, and those cases yield close

https://doi.org/10.1017/S0022112008003522 Published online by Cambridge University Press

agreement with direct simulations in terms of the wall shear stress. The use of the parabolic solution scheme described at the start of this section, or indeed any scheme, in the presence of such regions of reversed flow is of course essentially suspect. We do not address this here, although some progress is possible by use of windward differencing for instance.

An overall expansion of the vessel interiors is also seen in figure 5(*a–e*) where four daughters are nearly formed but actually only two because the approach towards the creation of the second and third carinas is overwhelmed by the vessel expansion. Three cases are examined as Γ is set to 1, 1/100, 1/300 in turn corresponding to varying values of Re in the ratio 1, 100, 300, in figures 5(*c–e*) which present the corresponding axial velocity u_{mid} in the mid-plane where z is zero on the same scale throughout in order to facilitate comparisons. Figure 5(*c*) has $\Gamma = 1$ and the motion does not reverse at all, in keeping with the effectively low flow rate, and the entire flow response is smooth. There is a gradual u_{mid} decrease to the saddle point of the carina, after which despite the fluid deceleration there is a smooth progress to the downstream end which is at $X = 2$. In figure 5(*b*) u_{cl} and π_1 are plotted versus X for this case, again showing the relative smoothness in u_{cl}, together with the axial pressure gradient remaining favourable throughout. A more severe velocity plunge to the carina's saddle point is observed in figure 5(*d*) for $\Gamma = 1/100$ and the solution exhibited flow reversal with $u < 0$ occurring at the outermost walls. Close to those walls a positive curvature of the velocity profiles is seen which is in agreement with the axial pressure gradient becoming adverse. Figure 5(*e*) has the same geometry but Γ is decreased to 1/300. Now the flow reverses at the outer walls sooner spatially as might be expected of the higher flow rate, with the curvature locally near walls remaining in essence as before: the subsequent analysis shows that inviscid dynamics can dominate globally but viscous–inviscid interaction enters locally to induce regular separation.

Figures 6 and 7 show results for four daughters, with Γ of unity. The vessel shapes are as shown in figure 6(*a*) and are similar to those of figure 5(*a*) but now H_2, H_3 are altered (to $0.5H_1$), so that three carinas are formed in spite of the general expansion of the vessels. Figure 6(*b*) gives u_{cl} and π_1 against X, showing that both are comparatively smooth, the axial pressure gradient is favourable throughout and the calculation proceeds to the downstream end satisfactorily. Axial velocity profiles u_{mid} at various X stations and axial velocity contours as given in figure 6(*c*) show that the motion remains entirely forward, consistent with the moderate flow rate, and the general response is smooth including the three noticeable plunges in u_{mid} on approaching each of the three carinas' saddle points, after which despite the fluid deceleration there is a gradual progress to the downstream end in each of the four daughters. Figure 7(*a–d*) gives the cross-plane velocity contours at various X stations. It can be seen that substantial swirling flow is produced although the whole flow behaviour is relatively smooth.

The results taken together tend to suggest among other features that the bulk of the flow solution through the three-dimensional geometry is determined quite accurately even if it is difficult to capture all the details near the onset of every carina and branching. We should add that in symmetric cases, with say two identical daughters, the two pressure responses π_1, π_2 being equal in the daughters makes the calculation easier there. Also in the daughters the downstream decay is seen to be relatively fast. Inertial responses which increase with decreasing Γ are seen to carry from the mother through into the daughters and axial separation in the sense of flow reversal can arise some way ahead of any carina: see also the next sections. Such reversal is due to a combination of shape effects and the flow rate. Generally at each branch

https://doi.org/10.1017/S0022112008003522 Published online by Cambridge University Press

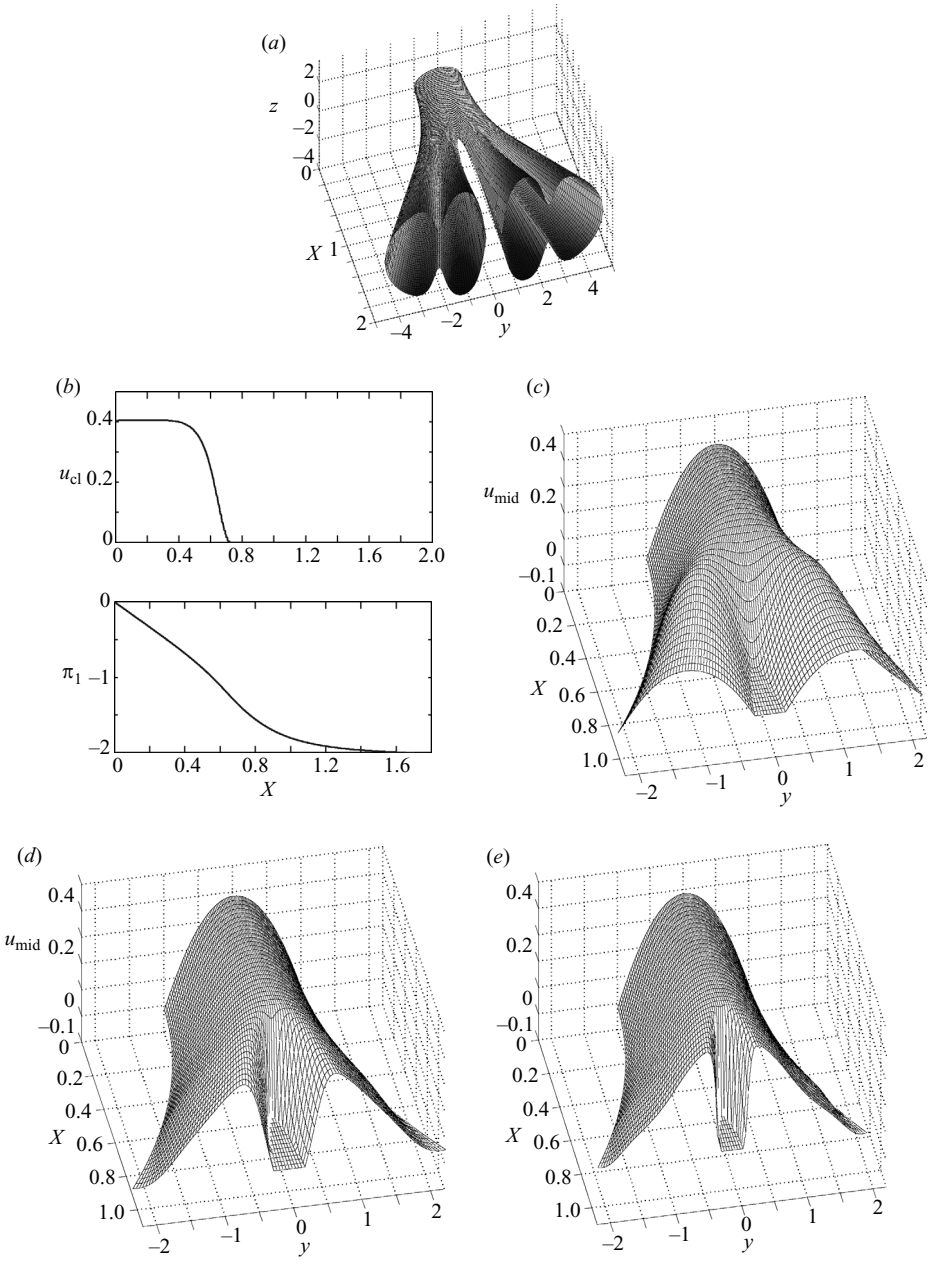


FIGURE 5. Effects of varying the flow rate, where the mother splits into two daughters with a further four grandaughter vessels nearly being formed. (*a*) Branching geometry, $h_1 = 2.8$, $h_2 = h_3 = 0.3h_1$. (*b*) u_{cl} and π_1 against X for (*c*). (*c*) Surface plot of the axial velocity u_{mid} in the plane $z = 0$ for $\Gamma = 1$. (*d*) As for (*c*) but with Γ decreased to 1/100. (*e*) As for (*c*) but with Γ decreased to 1/300.

junction the fluid is seen to flow *around* the effective obstacle made by the carina and branches, which is a specifically three-dimensional behaviour and not unlike that at wing–body junctions as studied by Seal *et al.* (1995*a*), Seal, Smith & Rockwell (1995*b*), Seal & Smith (1997), Marini & Smith (2002) and Smith & Gajjar (1984).

https://doi.org/10.1017/S0022112008003522 Published online by Cambridge University Press

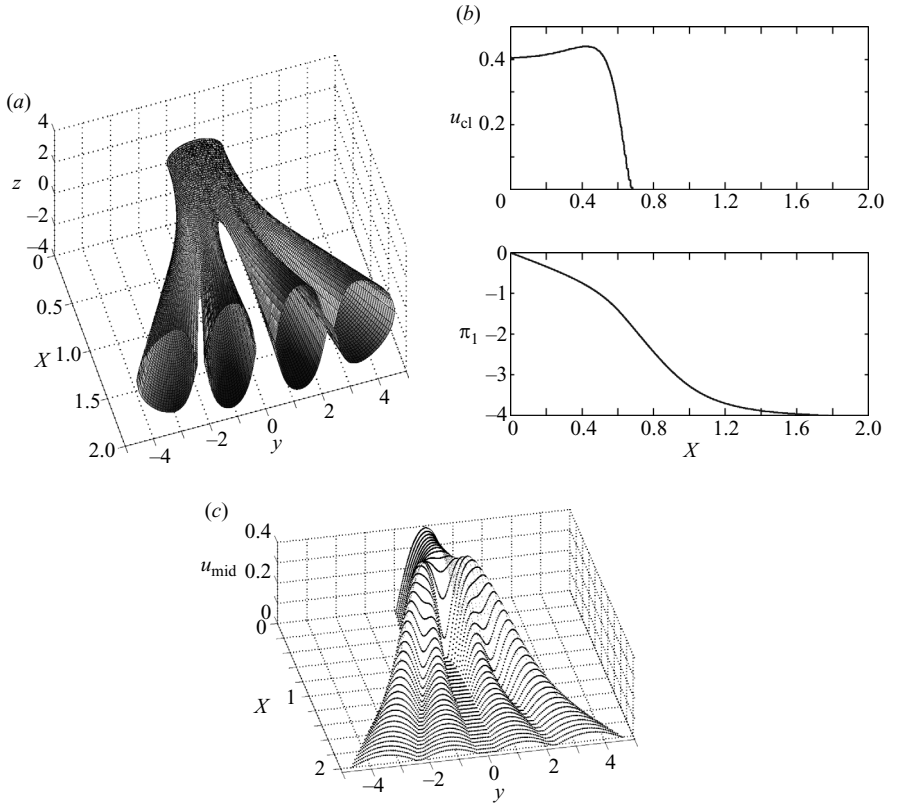


FIGURE 6. A case of a mother splitting into two daughters and then four grandaughters with $\Gamma = 1$, $h_1 = 2.8$, $h_2 = h_3 = 0.5h_1$. (*a*) Branching geometry. (*b*) u_{cl} and π_1 against X. (*c*) Surface plot of axial velocity u_{mid} in the plane $z = 0$.

Refined calculations were necessary in some cases, usually involving refinement in y, z close to branch junctions. The overall numerical findings lead into the analysis of the next two sections.

4. Analysis near the saddle point of a carina and branching

In the motion near a representative branch junction at some station $X = X_c$ there are two principal regions to consider in any search for an asymptotic structure for the solution on the assumption that $X - X_c$ is small. One is the core comprising the bulk of the flow where the typical y, z coordinates are of order unity for $X - X_c$ small and the other is close to the saddle point of the carina where $y - y_c$, $z - z_c$ are both additionally small, with the saddle point of the carina situated at $(y, z) = (y_c, z_c)$. In the numerical examples of the previous section, this region has $|z - z_c| \sim |y - y_c|^2$ because of the shape of the maximum pinch involved, so that $|z - z_c| \ll |y - y_c|$ and z derivatives dominate over y derivatives, while the axial shaping gives $|z - z_c|$ shrinking to zero like $(X_c - X)$ as $X \to X_c-$. Hence the local length scales are then given by $|z - z_c| \sim |X - X_c|$, $|y - y_c| \sim |X - X_c|^{1/2}$. Also the dominant pressure π_1 is expected to be regular in the axial direction, indicating the sizes of the major inertial, pressure gradient and viscous forces in the axial momentum balance to be $O(u^2/|X - X_c|)$, $O(1)$, $O(|u|/|X - X_c|^2)$ respectively; these sizes imply that $|u| \sim |X - X_c|^2$ and so the viscous and pressure gradient effects overwhelm the inertial ones.

https://doi.org/10.1017/S0022112008003522 Published online by Cambridge University Press

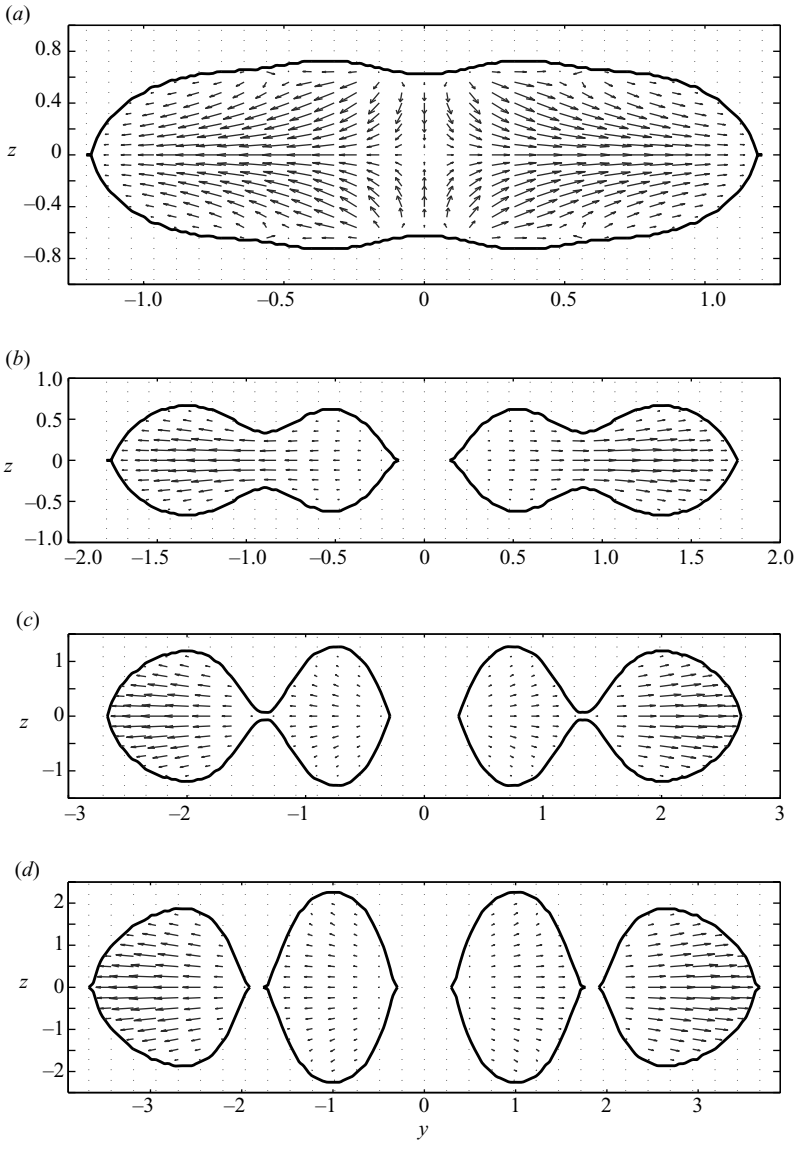


FIGURE 7. A case of a mother splitting into two daughters and then four grandaughters with $\Gamma = 1$, $h_1 = 2.8$, $h_2 = h_3 = 0.5h_1$. Secondary flow vectors of (V, W) at (*a*) $X = 0.4$, (*b*)0.8, (*c*) 1.2 and (*d*) 1.6 respectively.

The ordering here for u is equivalent to $|u| \sim |z - z_c|^2$, we note. In what follows we allow for a more general carina shape, as illustrated in figure 8, whilst maintaining the constraint $|z - z_c| \ll |y - y_c|$.

Whatever the details close to the carina's saddle point, the core solution proceeds in essentially regular form in the axial direction, for y, z of order unity and with $X - X_c = \varepsilon\zeta$, with ζ of order unity defining the expansion parameter ε,

$$[u, V, W] = [u_0, V_0, W_0](y, z) + \varepsilon\zeta\,[u_1, V_1, W_1](y, z) + \cdots, \tag{4.1a}$$

$$[\pi_1, \pi_2] = [p_0, P_0(y, z)] + \varepsilon\zeta\,[p_1, P_1(y, z)] + \cdots, \tag{4.1b}$$

https://doi.org/10.1017/S0022112008003522 Published online by Cambridge University Press

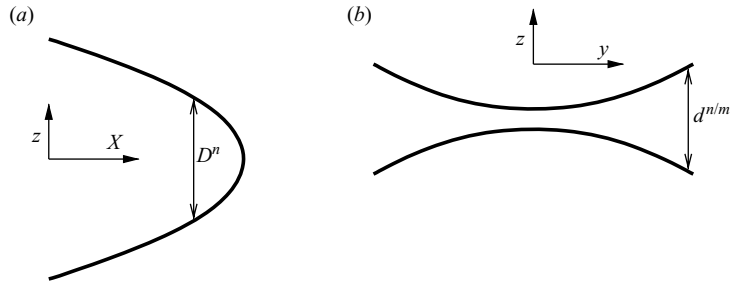


FIGURE 8. General local shapes near a carina: (*a*) as seen in the (X, z)-plane with the distance D denoting $X_c - X$; (*b*) as seen in the (y, z)-cross-sectional plane with the distance d denoting $y - y_c$. The saddle point shapes in the computations correspond to $n = 1$, $m = 1/2$.

with $u_0(y, z)$ being the local axial velocity profile. Substitution of (4.1*a*, *b*) into the governing system (2.3*a*) to (2.3*d*) yields

$$u_1 + V_{0y} + W_{0z} = 0, \tag{4.2a}$$

$$u_0 u_1 + V_0 u_{0y} + W_0 u_{0z} = -p_1 + \Gamma \Delta u_0, \tag{4.2b}$$

$$u_0 V_1 + V_0 V_{0y} + W_0 V_{0z} = -\partial P_0/\partial y + \Gamma \Delta V_0, \tag{4.2c}$$

$$u_0 W_1 + V_0 W_{0y} + W_0 W_{0z} = -\partial P_0/\partial z + \Gamma \Delta W_0, \tag{4.2d}$$

which act to control u_1, V_0, W_0 and so on, given the u_0 profile, p_0 and p_1, which are obtained in an integrated fashion on all the flow properties upstream of the branch junction.

The generalized saddle point region here is shaped as in figure 8 and has

$$y - y_c = \varepsilon^m \eta, \qquad z - z_c = \varepsilon^n \xi, \tag{4.3a}$$

$$[u, V, W] = [\varepsilon^{2n} U_\beta, \varepsilon^{2n+m-1} V_\beta, \varepsilon^{3n-1} W_\beta](\zeta, \eta, \xi) + \cdots, \tag{4.3b}$$

$$\pi_2 = \varepsilon^{2m-1} \pi_{2\beta}(\eta, \xi) + \cdots, \tag{4.3c}$$

together with π_1 remaining as in (4.1*b*) of course. The scalings here are derived from an argument similar to that presented near the start of this section but in the context of this generalized geometry. The uniformity of π_1 over the cross-section plays an important role in determining the orders of magnitude, as anticipated. The assumption is that the powers m, n satisfy $n > m > 0$ so that $|z - z_c| \ll |y - y_c|$. Substitution into (2.3*a*) to (2.3*d*) now yields in effect the controlling equations

$$\frac{\partial U_\beta}{\partial \zeta} + \frac{\partial V_\beta}{\partial \eta} + \frac{\partial W_\beta}{\partial \xi} = 0, \tag{4.4a}$$

$$0 = -p_1 + \Gamma \frac{\partial^2 U_\beta}{\partial \xi^2}, \tag{4.4b}$$

$$0 = -\frac{\partial \pi_{2\beta}}{\partial \eta} + \Gamma \frac{\partial^2 V_\beta}{\partial \xi^2}, \tag{4.4c}$$

$$0 = -\frac{\partial \pi_{2\beta}}{\partial \xi}, \tag{4.4d}$$

https://doi.org/10.1017/S0022112008003522 Published online by Cambridge University Press

subject to the wall conditions of no slip,

$$U_\beta = V_\beta = W_\beta = 0 \text{ at } \xi = \xi_+ = \alpha_1|\zeta|^n + \alpha_2|\eta|^{n/m} \text{ and } \xi = \xi_- = -\alpha_3|\zeta|^n - \alpha_4|\eta|^{n/m}, \tag{4.4e}$$

where the local shape constants α_1 to α_4 are positive. The constants α_1, α_2 apply to the upper wall approaching the carina's saddle point and α_3, α_4 to the lower. The computations have symmetry such that $\alpha_1 = \alpha_3$ and $\alpha_2 = \alpha_4$, incidentally, and $n = 1$, $n/m = 2$. This wall geometry could be made still more general locally, within the constraints set by the scalings (4.3*a*).

The solution of (4.4*a*–*e*) has velocity components described by

$$2\Gamma U_\beta = -p_1(\xi_+ - \xi)(\xi - \xi_-), \tag{4.5a}$$

$$2\Gamma V_\beta = -\frac{\partial \pi_{2\beta}}{\partial \eta}(\xi_+ - \xi)(\xi - \xi_-), \tag{4.5b}$$

$$\begin{aligned} 2\Gamma W_\beta = &-\frac{\partial^2 \pi_{2\beta}}{\partial \eta^2}\left\{\frac{(\xi^3 - \xi_+^3)}{3} - (\xi_+ + \xi_-)\frac{(\xi^2 - \xi_+^2)}{2} + \xi_+\xi_-(\xi - \xi_+)\right\} \\ &- \frac{\partial \pi_{2\beta}}{\partial \eta}\left\{-\frac{\partial(\xi_+ + \xi_-)}{\partial \eta}\frac{(\xi^2 - \xi_+^2)}{2} + \frac{\partial(\xi_+\xi_-)}{\partial \eta}(\xi - \xi_+)\right\} \\ &- p_1\left\{-\frac{\partial(\xi_+ + \xi_-)}{\partial \zeta}\frac{(\xi^2 - \xi_+^2)}{2} + \frac{\partial(\xi_+\xi_-)}{\partial \zeta}(\xi - \xi_+)\right\}, \end{aligned} \tag{4.5c}$$

with the constant p_1 determined from the upstream behaviour in the core, see (4.1*b*), while the pressure gradient correction appearing in (4.5*b*, *c*) is given by

$$H^3 \frac{\partial \pi_{2\beta}}{\partial \eta} = -p_1 \int \frac{\partial(H^3)}{\partial \zeta}\, \mathrm{d}\eta, \tag{4.5d}$$

to within an additive function of ζ as could be anticipated in view of the original pressure form in (2.2*b*). The effective gap width $H = (\xi_+ - \xi_-)$ here is known. Equation (4.5*d*) is consistent with the Reynolds lubrication equation, as expected. We notice from (4.4a) that $\mathrm{sgn}(U_\beta) = -\mathrm{sgn}(p_1)$ throughout the gap. Further the local behaviour is inherently three-dimensional in that p_1 determines the axial velocity U_β (via (4.4*b*)) which then acts to fix the crossflow velocities and pressure through the continuity balance (4.4*a*) and the major crossflow momentum effect (4.4*c*).

An alternative analysis of the flow in this carina region is to look for a similarity solution in the limit of small $|X - X_c|$ using the variables $\eta = (y - y_c)/|X - X_c|^m$ and $\xi = (z - z_c)/|X - X_c|^n$. The conclusions are identical to those obtained here. We adopt this approach, using similarity variables, in the analysis of the region for large flow rates in the next section and in the Appendix.

There is clear tie-in with the results of the computations. The y-variation of u_{mid}, in particular locally near the saddle point region, should be like y^4 according to the analysis in (4.3*a*)–(4.5*d*) and this is indeed in line with the local behaviour in figure 2(*c*). Also the distinction between core and saddle point region flow seems apparent throughout the results of the previous section, in particular in the local plunges of the axial velocity component towards zero near the saddle point of the carinas in the results of figures 2, 3, 5 and 6 compared with the milder developments in the cores away from the carina's saddle point. A quantitative comparison between the

https://doi.org/10.1017/S0022112008003522 Published online by Cambridge University Press

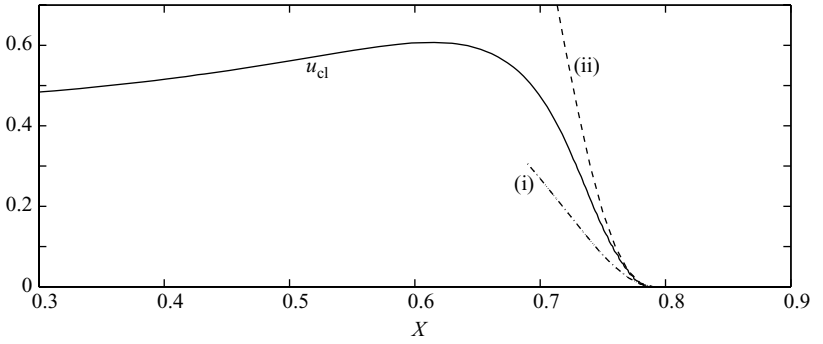


FIGURE 9. Comparison of u_{cl} (solid line) with the near-carina analysis for the case $\Gamma = 1$ using the geometry given in figure 2. (i) leading-order asymptotic solution; (ii) next-order asymptotic solution.

computations and near-carina analysis of this section is presented in figure 9 using the geometry given in figure 2(*a*). From (4.4*b*), the leading-order three-dimensional lubrication effect approaching the saddle point of the carina predicts that the centreline axial velocity $u_{cl} = u(X, 0, 0)$ behaves as

$$u_{cl}(X) \sim -\frac{\partial \pi_1}{\partial X}\frac{(\alpha_1|\zeta|)^2}{2\Gamma} \sim -\frac{\partial \pi_1}{\partial X}\frac{z_{upper}(X,0)^2}{2\Gamma} \quad \text{as } X \to X_c, \tag{4.6}$$

where $z_{upper}(X, y)$ from equation (3.1) gives the position of the vessel wall. For this particular geometry case, using (4.4*e*), we have that

$$z_{upper} = \alpha_1(X_c - X) + \alpha_2(y - y_c)^2 + O(|X - X_c|(y - y_c)^2), \tag{4.7}$$

as $(X, y) \to (X_c, y_c)$. Spanwise viscous effects can be incorporated by including the next-order $\partial^2 U_\beta/\partial\eta^2$ term in equation (4.4*b*), the magnitude of which is reduced compared to the $\partial^2 U_\beta/\partial\xi^2$ term owing to the relative y–z slenderness ratio of the carina's saddle point. This leads us to obtain a next-order approximation for the centreline velocity of the form

$$\begin{aligned} u_{cl}(X) &\sim -\frac{\partial \pi_1}{\partial X}\frac{(\alpha_1|\zeta|)^2}{2\Gamma}(1 + 2\alpha_1|\zeta|\alpha_2) \\ &\sim -\frac{\partial \pi_1}{\partial X}\frac{z_{upper}(X,0)^2}{2\Gamma}\left(1 + z_{upper}(X,0)\frac{\partial^2}{\partial y^2}z_{upper}(X,0)\right) \quad \text{as } X \to X_c. \end{aligned} \tag{4.8}$$

Both leading-order (4.6) and next-order (4.8) comparisons are shown for the case where $\Gamma = 1$ using the values of u_{cl} and π_1 obtained from the computations. Note that the computations appear to confirm the validity of the analysis as the carina's saddle point is approached (here $X_c = 0.79$), with much improved agreement once higher-order spanwise viscous effects are included.

We should remark here that the linear response of the core flow in (4.1*a*, *b*), arising despite the $O(1)$ changes in cross-section brought about by the branching overall, is similar to that described by Ovenden, Smith & Wu (2008) and Tadjfar & Smith (2004). Again, it is noticeable that although the regime (*b*) mentioned in § 2 is the one to which attention has been directed, there are clearly elements of both (*a*) and (*c*) also in the local response; regime (*c*) is addressed in some detail in the next section. The analytical account in (4.1*a*)–(4.5*d*) of the present response also shows that forward ($u > 0$) or reversed ($u < 0$) motion is possible near the carina's saddle

https://doi.org/10.1017/S0022112008003522 Published online by Cambridge University Press

point, a matter which (somewhat surprisingly perhaps) depends solely on the sign of the axial pressure gradient p_1 locally which in turn depends on the global flow properties upstream.

There are several relevant possible extensions to suggest immediately. First, various types of wall shape can be accommodated in the formulation (4.1*a*)–(4.4*d*). For instance the description of the flow solution for $X = X_c+$, just after the saddle point, is similar as described below, and indeed entire branching shapes can be accommodated within this formulation. Second, the axial pressure gradient at the carina, p_1 in (4.1*b*), is taken to be order one in the above, but if it is much larger, of $O(\varepsilon^{-1})$, over a small distance $O(\varepsilon)$ from the carina's saddle point in effect, then the saddle point region becomes nonlinear. This then yields dual solutions and other properties as discussed in the Apendix. Third, reasoning along the following lines supports the occurrence of reversed flow approaching a carina's saddle point accompanied by a positive pressure gradient. Imagine a predominantly axisymmetric mother flow, for which a two-dimensional subset is known to hold near the outer wall as in Smith (1976) and yields a regular flow separation at some $X = X_{\text{sep}}$ with positive pressure gradient, for example for a cornered dilation. This positive pressure gradient effect feeds all the way across the axisymmetric mother tube. If then a smallish three-dimensional carina positioned downstream of that regular two-dimensional separation is added, within the wall layer near that outer wall, beyond some $X = X_1$ downstream of X_{sep}, the structure described in the analysis above is obtained.

Importantly however, the main physical point of this paper is that the axial pressure gradient (p_1) which drives the axial flow in the saddle point region is determined by the bulk of the branching flows (the cores) and can be locally positive or negative. The sign is determined through an interplay of inertial effects, genuinely three-dimensional behaviour and the global network properties discussed in § 1. The uniformity of the main pressure gradient p_1 over the cross-section essentially means that viscous forces and the underlying momentum carry the core on forward into the daughters while locally near the saddle point lubrication properties hold. The sign of that gradient dictates whether flow is reversed close to the saddle point or not, within the present regime. (This should be compared with the lubrication subcase (*a*) which has negligible inertia and cannot allow a positive axial pressure gradient unless the total tube flow is reversed.)

The reasoning above has been about the flow response just ahead of the carina. Virtually the same reasoning applies to the flows just downstream, in the entry to the daughters where $X > X_c$. The particular wall shapes in (4.4*e*), (4.5*a*–*c*) for instance can still hold subject to the requirement that in the flow solution η is restricted to the fluid-gap interval of course.

5. Behaviour for high flow rates

Relatively high flow rates produced by an increased Reynolds number Re for a fixed geometry correspond to small values of Γ as mentioned earlier. Clearly from the governing equations (2.3*a*) to (2.3*d*) that points primarily to the inviscid case under regime (*c*) and hence to driving a virtually inviscid fluid to the verge of the carina. We now investigate this, looking for a similarity solution to the governing equations.

To leading order the equations holding are (2.3*a*–*d*) with

$$\Gamma = 0, \tag{5.1}$$

https://doi.org/10.1017/S0022112008003522 Published online by Cambridge University Press

and in the absence of any large-scale separation the tangential flow condition

$$W = uf_X + Vf_y \quad \text{on} \quad z = f(X, y) \tag{5.2}$$

replaces the no-slip constraint if the walls are expressed as $z = f(X, y)$ say, and likewise for other wall expressions. The inviscid system corresponding to (5.1) is subject to a general viscous correction of order Γ as far as the fuller original governing equations are concerned and to the presence of thin viscous wall layers.

At the onset of the carina now, as $X \to X_c-$, we expect that as in the fuller case of the previous section the regular expansion (4.1*a*, *b*) continues to hold in the core and is associated with the axial pressure gradient $\pi_1'(X)$ remaining finite, yielding the properties in (4.2*a–d*) with Γ replaced by zero. Closer to the carina's saddle point reasoning about the orders of magnitude here and with the saddle point geometry described by the case $n = 1$, $m = 1/2$, suggests the behaviour

$$y - y_c = |X - X_c|^{1/2}\eta, \quad z - z_c = |X - X_c|\xi, \tag{5.3a}$$

$$(u, V, W) = (|X - X_c|^{1/2}u_\gamma, V_\gamma, |X - X_c|^{1/2}W_\gamma)(\eta, \xi) + \cdots \tag{5.3b}$$

$$\pi_2 = \pi_{2\gamma} + \cdots. \tag{5.3c}$$

The inviscid system involving (5.1) therefore gives the three-dimensional thin-layer equations

$$-\tfrac{1}{2}(u_\gamma - \eta\partial u_\gamma/\partial\eta - 2\xi\,\partial u_\gamma/\partial\xi) + \partial V_\gamma/\partial\eta + \partial W_\gamma/\partial\xi = 0, \tag{5.4a}$$

$$-\tfrac{1}{2}u_\gamma(u_\gamma - \eta\partial u_\gamma/\partial\eta - 2\xi\,\partial u_\gamma/\partial\xi) + V_\gamma\partial u_\gamma/\partial\eta + W_\gamma\partial u_\gamma/\partial\xi = -\pi_1'(X_c), \tag{5.4b}$$

$$-\tfrac{1}{2}u_\gamma(-\eta\partial V_\gamma/\partial\eta - 2\xi\,\partial V_\gamma/\partial\xi) + V_\gamma\partial V_\gamma/\partial\eta + W_\gamma\partial V_\gamma/\partial\xi = -\partial\pi_{2\gamma}/\partial\eta, \tag{5.4c}$$

$$\partial\pi_{2\gamma}/\partial\xi = 0, \tag{5.4d}$$

with (5.2) leading to

$$W_\gamma = -u_\gamma + 2\eta V_\gamma \tag{5.4e}$$

at the wall given, in normalized terms, by

$$\xi = 1 + \eta^2. \tag{5.4f}$$

Consider the solution for η small. By symmetry with respect to η

$$u_\gamma \sim 1, \quad W_\gamma \sim 1, \quad \text{but} \quad V_\gamma \sim \eta V_{\gamma 1}, \quad \pi_{2\gamma} \sim \pi_{2\gamma 0} + \eta^2\pi_{2\gamma 2} \tag{5.5}$$

say, and so (5.4*a–f*) reduce to the form

$$-\tfrac{1}{2}(u_\gamma - 2\xi u_\gamma') + V_{\gamma 1} + W_\gamma' = 0, \tag{5.6a}$$

$$-\tfrac{1}{2}u_\gamma(u_\gamma - 2\xi u_\gamma') + W_\gamma u_\gamma' = -\pi_1'(X_c), \tag{5.6b}$$

$$-\tfrac{1}{2}u_\gamma(-V_{\gamma 1} - 2\xi V_{\gamma 1}') + V_{\gamma 1}^2 + W_\gamma V_{\gamma 1}' = -2\pi_{2\gamma 2}, \tag{5.6c}$$

with $\pi_{2\gamma 2}$ being a constant and

$$W_\gamma = -u_\gamma \quad \text{at} \quad \xi = 1, \quad u_\gamma = V_{\gamma 1}' = W_\gamma = 0 \quad \text{at} \quad \xi = 0, \tag{5.6d}$$

using symmetry in ξ. The required solution is simply

$$u_\gamma = c_1, \quad V_{\gamma 1} = c_2, \quad W_\gamma = -c_1\xi, \tag{5.7}$$

corresponding to the three-dimensional flow being squeezed in the z-direction by the presence of the converging walls and slowing down in the axial direction but escaping

https://doi.org/10.1017/S0022112008003522 Published online by Cambridge University Press

in the positive and negative y-directions. The constants c_1, c_2 above are such that $2\pi_1'(X_c) = c_1^2$, $2c_2 = 3c_1$, $4\pi_{2\gamma 2} = -c_1c_2 - 2c_2^2$, from (5.6$a$–$c$), confirming as one might expect that the axial pressure gradient must be positive locally whereas the pressure gradient in the spanwise y-direction is negative as fluid accelerates away from the saddle point blockage effect as if to start to skirt around it. A similar limiting solution but with $u_\gamma \sim \eta$, $V_\gamma \sim 1$, $W_\gamma \sim \eta$ and $\xi \sim \eta^2$ holds at large η as the core is approached. This implies that the axial velocity u itself increases to the order of unity in the core, in keeping with the form assumed earlier in the present paragraph.

Viscous effects must come back into play eventually, closer to the saddle point, since lubrication dominates always for the broad regime (b) of which (c) is a subset. When and how the necessary further adjustment takes place even closer to the carina's saddle point is as follows. The orders of magnitude involved here have the typical axial inertia contribution $u\partial u/\partial X$ and the pressure gradient π_1' being of order unity whereas the major diffusion term in the axial direction is $\Gamma\partial^2 u/\partial z^2$ which is estimated to be of order $\Gamma|X - X_c|^{-3/2}$ because of the scales of u, z in (5.3a, b). Hence the viscous effects become comparable with the previously dominant inviscid ones when $|X - X_c|$ is as small as $\Gamma^{2/3}$, at which stage the sizes of the velocities, pressure and lengths are represented by

$$(u, V, W, \pi_1', \pi_2) \sim (\Gamma^{1/3}, 1, \Gamma^{1/3}, 1, 1) \tag{5.8a}$$

while

$$(X - X_c, y - y_c, z - z_c) \sim (\Gamma^{2/3}, \Gamma^{1/3}, \Gamma^{2/3}), \tag{5.8b}$$

according to the same ordering argument. In consequence the governing system (2.3a–d) now reduces to the form of a three-dimensional viscous–inviscid thin layer,

$$\nabla \cdot \boldsymbol{u} = 0, \tag{5.9a}$$

$$(\boldsymbol{u} \cdot \nabla)u = -\pi_1'(X) + \partial^2 u/\partial z^2, \tag{5.9b}$$

$$(\boldsymbol{u} \cdot \nabla)V = -\partial\pi_2(X, y)/\partial y + \partial^2 V/\partial z^2, \tag{5.9c}$$

with the z-momentum balance requiring $\partial\pi_2/\partial z$ to be effectively zero, so that the unknown pressure correction π_2 depends on X, y only locally. The no-slip conditions apply here in full at the local wall surface and matching to the core holds at large positive or negative $|y - y_c|$ with the core determining π_1' as previously.

The thin-layer response (5.8a)–(5.9c) acts to smooth the flow behaviour though on a shortened axial length scale. The viscous–inviscid adjustment there agrees as required with the predominantly inviscid behaviour which describes the motion slightly upstream as in (5.1)ff, and then leads into the lubrication account of the previous section which applies for any value of Γ at the onset of the saddle point at smaller $|X - X_c|$ values and which is contained within the reduced system (5.9a–c).

Elements of the present multi-structured flow response can be seen in the earlier computations of § 3 for decreasing Γ values. The results on relatively abrupt carinas or higher flow rates for which inviscid theory tends to apply at first hint at the successive viscous–inviscid adjustment on a shorter scale just described, with the square-root property in the axial velocity component u according to (5.3b) being indicated in the results. Thus there are signs of inertial dominance in $u_{\rm cl}$ for Γ of 1/100 in figure 3(b) in particular, while although figures 5(e) and 6(b) have smoother $u_{\rm cl}$ forms for Γ of unity there are still signs of an inviscid square-root (of distance) response in $u_{\rm cl}$ prior to the final parabolic distance-squared plunge. Altogether, then, the general result of § 4 remains true here as essentially the same viscous domination applies at the

https://doi.org/10.1017/S0022112008003522 Published online by Cambridge University Press

verge of the carina's saddle point even though there is virtually inviscid evolution beforehand.

6. Further comments

An immediate point to make is that all of the dynamics in the present model of branching flows is three-dimensional. That includes the spatial evolution of the velocity profiles in each vessel from the upstream entrance to the next carina and branch junction, since the spatial evolution is modelled by a longitudinal vortex system in every case in view of the assumed slenderness of the vessels. There is an interplay between the non-dimensional axial scale involved and the 'viscous', or more accurately the viscous–inviscid, length scale of order Re where Re is the Reynolds number. Although it may be argued that the viscous length scale is rather long in terms of some realistic upstream shapings, the above interplay forms a central starting point and allows analysis for relatively short length scales anyway, and also the Reynolds number is not necessarily very large in reality. The inherent *three-dimensionality* of the dynamics is further evident in the analysis in the previous two sections. At each branch junction there is a new *inertial effect* (in addition to a usual viscous one) as fluid is driven from the mother into the daughter tubes, an effect which arises as a result of the spatial evolution upstream in the mother, i.e. it is global, which produces an axial pressure gradient that can be favourable or adverse and which leads to forward or reversed flow respectively close to the carina's saddle point. The inertial effect continues into the cores of the daughters, giving longitudinal vortices downstream as found by Comer *et al.* The property that in general there can occur positive (adverse) or negative (favourable) axial pressure gradients should first be compared with the lubrication-like flows which apply at reduced Reynolds numbers or equivalently over non-dimensional length scales much larger than the viscous length scale; these flows have negligible inertia and cannot allow positive axial pressure gradients unless the total flow is reversed. Second, the predominantly inviscid theory of the previous section supports the important role of the core and its difference from the more localized saddle point region in terms of the inertial effect. The saddle point flow reversal occurs despite the largeness of Re and the forward continuation of the bulk of the motion.

Both the computational and the analytical results further illustrate the dependence on Reynolds number and on the various area-expansion ratios examined and show that significant swirling flow is produced by the branchings, a feature which is important for medical applications involving particle delivery and for theoretical analysis on the flow downstream. All the predictions are within the limitations of the present model as described above and pressure jumps (Smith, *et al.* 2003*b*) at the branch junctions, which can be smoothed out over shorter length scales, are assumed to be absent here.

The current findings appear to support those of Comer *et al.* (2001*a*, *b*). The present model approach is different of course, being less full in terms of equations but allowing more analysis in certain cases, and many daughter vessels can be accommodated here. It would be interesting to tackle the lubrication limit (*a*) of comparatively low flow rates throughout the three-dimensional system, which corresponds locally to the case of m, n being equal in § 4 and leads to a Poisson-type problem for the pressure, as well as tackling the high flow rate limit (*c*). Another advantage of the current model is that it can incorporate any cross-sectional shapes, in principle, even the multiply branching ones of most medical concern.

https://doi.org/10.1017/S0022112008003522 Published online by Cambridge University Press

Concerning the carina or near-carina shape itself, this has usually been taken to be parabolic in the cross-section just upstream as in the particular cases studied in §§ 3–5. A marginal shape of linear cross-sectional form, with the parabolic part disappearing at the onset of the carina, seems at least equally relevant in physical terms and it also corresponds to having m, n equal in § 4, leading to a distinct Poisson-type effect. Again, it is worth mentioning that the branching and saddle point act locally as small perturbations in the present setting as shown in the previous two sections, despite the large changes in cross-sectional shape elsewhere. The Appendix considers more pronounced effects taking place near the saddle point of a carina.

Concerning extensions of the theory, the three-dimensional geometry involved is similar to that occurring in collapsed tubes as sketched in Grotberg & Jensen's (2004) figure 2 for example, as mentioned in the introduction, with contact of opposite tube walls. That paper also notes Bertram & Godbole's (1997) visualizations of the steady three-dimensional motion downstream, including twin jets with flow reversal between them. The flow reversal seems to tie in qualitatively with the present analysis in §§ 4, 5.

Modelling of blockages in tubes provides another biomedical motivation. Indeed, if the effective obstruction is of finite length, as in collapsed tube or blockage scenario, the present three-dimensional system can be marched past the obstruction, into the wake, using regimes (a–c) of § 2 for Re/L large (quasi-inviscid flow), Re/L of $O(1)$ (viscous–inviscid flow) or Re/L small (the lubrication extreme).

Different branching geometries are also of significant interest, for instance a mother of circular cross-section but with a small side hole as daughter added in a region near the outer wall. The region can have flow which is totally lubricating or totally inviscid as in §§ 4, 5. Also, generalizing § 4 we see that the argument for the local saddle point response essentially remains intact provided the axial pressure remains finite there, no matter what the gradient. Increasing axial pressure gradient is likely to be produced by the presence of one small daughter as just described or by many daughters, which leads into the work the Appendix on nonlinear saddle point interactions. There are a host of other slender three-dimensional flow problems worthy of study: on wall roughness, curves, corners, expansions, contractions and their effects on suppression of reversal for example, and on the tortuous three-dimensional vessel paths observed in the Circle of Willis, lung airways, cochlear, urinary tracts and elsewhere. The present geometries can be made non-symmetric as we have seen in the upstream part, after which unequal pressure gradients in the daughters have to be accommodated. A question arises here as to whether it is possible or desirable to design three-dimensional vessels producing two-dimensional flow. Allied questions and extensions concern other general local shapes of bifurcation, unsteadiness, elastic wall effects, networks of vessels, and particle deposition or glue spreading applications.

Thanks are due to EPSRC for support of N.C.O. during 2003–5, to the UCL Medical Modelling group, especially Neil Kitchen, for their encouragement and interest, to Rafael Pacheco for pointing out two references, and to Mehran Tadjfar for his interest. We are also very grateful to the referees for their comments and suggestions.

Appendix. Nonlinear saddle point behaviour

If the axial pressure gradient near the saddle point of the carina is as large as the inverse of distance then the local flow solution takes the form, extended from

https://doi.org/10.1017/S0022112008003522 Published online by Cambridge University Press

that in (4.3*a–c*),

$$y - y_c = |X - X_c|^{1/4}\eta, \quad z - z_c = |X - X_c|^{1/2}\xi, \tag{A 1}$$

$$(u, V, W) = (u_*, |X - X_c|^{-3/4}V_*, |X - X_c|^{-1/2}W_*)(\eta, \xi) + \cdots, \tag{A 2}$$

$$\pi_1' = |X - X_c|^{-1}Q_* + \cdots, \quad \pi_2 = |X - X_c|^{-3/2}\pi_* + \cdots, \tag{A 3}$$

for the case of a saddle point shape with $m = 1/4$, $n = 1/2$ locally. Here π_* must be independent of ξ. Near the symmetry line $\eta = 0$ where V_* is linear in η and the variation in the pressure term π_* is quadratic, say $V = \eta$ and $\pi = \eta^2$ respectively, the governing equations from (2.2*a–d*) are then

$$\tfrac{1}{2}\xi \mathrm{d}u_*/\mathrm{d}\xi + V_{**} + \mathrm{d}W_*/\mathrm{d}\xi = 0, \tag{A 4}$$

$$\left(\tfrac{1}{2}\xi u_* + W_*\right)\mathrm{d}u_*/\mathrm{d}\xi = -Q_* + \mathrm{d}^2u_*/\mathrm{d}\xi^2, \tag{A 5}$$

$$\left(\tfrac{1}{2}\xi u_* + W_*\right)\mathrm{d}V_{**}/\mathrm{d}\xi + (u_* + V_{**})V_{**} = -2\pi_{**} + \mathrm{d}^2V_{**}/\mathrm{d}\xi^2, \tag{A 6}$$

which are subject to the boundary conditions of no slip at the walls and of symmetry with respect to ξ, so that

$$u_* = V_{**} = W_* = 0, \quad \text{at} \quad \xi = 1, \tag{A 7}$$

$$\mathrm{d}u_*/\mathrm{d}\xi = \mathrm{d}V_{**}/\mathrm{d}\xi = W_* = 0, \quad \text{at} \quad \xi = 0, \tag{A 8}$$

where the walls are normalized to be a distance 2 apart in terms of ξ without loss of generality. The axial pressure coefficient Q_* can be taken as known from the core as in §§ 4, 5 whereas the effective cross-sectional pressure coefficient π_{**} is to be found for a given Q_*, or equivalently vice versa.

Calculations of the nonlinear ordinary differential system (A 4)–(A 8) as presented in figure 10(*a–c*) show that flow solutions exist only over a finite range of Q_* values and the corresponding π_{**} range is bounded above by a positive critical value. Also, there is non-uniqueness with two π_{**} solutions existing for a given Q_* value and vice versa in general. In particular there are two solutions for Q_* when π_{**} is set as zero: one has zero Q_* and corresponds to the flow regime addressed in § 4 while the other has a positive Q_* value.

Asymptotic properties support the above findings. First for small π_{**}, Q_* it is found from (A 4)–(A 8) that

$$\pi_{**} \sim \tfrac{1}{4}Q_*, \tag{A 9}$$

which is in agreement with the linear response in (4.3*a*)–(4.5*d*). Second, for large negative π_{**} the upper branch as in figure 10(*b*) where Q_* is positive has the inviscid majority of the flow, being given by

$$[V_{**}, W_*] \sim A[-n\pi\cos(n\pi\xi), \sin(n\pi\xi)], \quad u_* = B, \tag{A 10}$$

$$A = (2|\pi_{**}|)^{1/2}/(n\pi), \quad n = 1, \tag{A 11}$$

to satisfy (A 8), where the constant B is negative (corresponding to reversed axial flow) and much less than A in magnitude. Together with this there is by virtue of (A 7) a wall layer near $\xi = 1$ of scaled width $|\pi_{**}|^{-1/4}$ in which a quasi-planar front-stagnation-point form applies in terms of the skewed velocity component $(u_* + W_*)/2$, while u_* itself grows logarithmically negative in the upper reaches of the wall layer to match with (A 10). Third, for large negative π_{**} values but on the lower branch as

https://doi.org/10.1017/S0022112008003522 Published online by Cambridge University Press

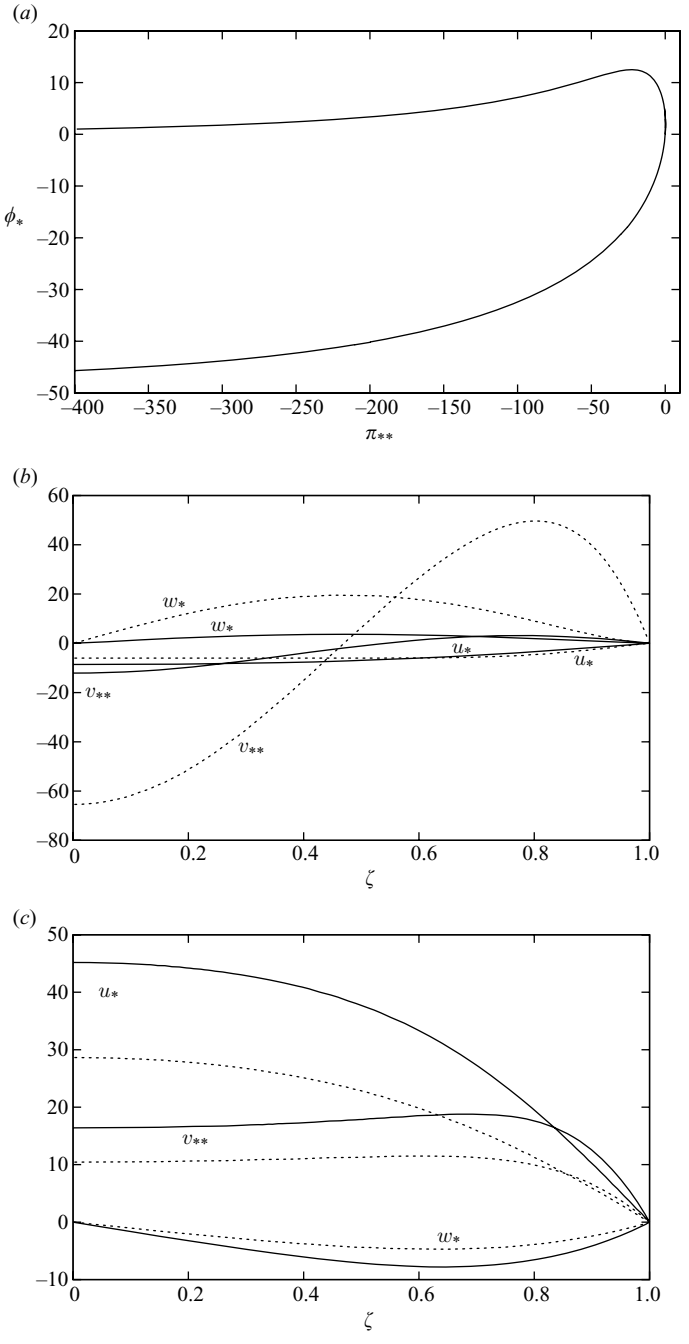


FIGURE 10. Nonlinear saddle point behaviour. (*a*) Effective axial pressure coefficient Q_* against cross-section pressure coefficient π_{**}. The lower branch of the solution reaches a minimum $Q_* \approx -47$ at $\pi_{**} - 1000$ and, proceeding leftward, increases to $Q_* \approx -41$ at $\pi_{**} = -2000$. (*b*) Scaled velocity profiles along the upper branch. Solid: $\pi_{**} = -2000$. Dashed: $\pi_{**} = -60$. (*c*) Scaled velocity profiles along the lower branch. Solid: $\pi_{**} = -500$. Dashed: $\pi_{**} = -200$.

https://doi.org/10.1017/S0022112008003522 Published online by Cambridge University Press

in figure 10(*c*) where Q_* is negative the asymptote is found after some analysis to develop according to

$$[u_*, V_{**}] \sim [2, 1]\left(\tfrac{2}{3}|\pi_{**}|\right)^{1/2}, \quad W_* \sim -\tfrac{1}{2}u_*\xi, \tag{A 12}$$

within the inviscid bulk, where the axial motion remains forward. Now the required viscous wall layer turns out to be fully three-dimensional, matching with the three non-zero edge values of velocity in (A 12) evaluated at $\xi = 1-$; details of the wall layer solution here may be requested from the authors. The behaviours in (A 9)–(A 12) tie in well with the calculations in figure 10(*a–c*) as well as with the trends found from the earlier figures.

REFERENCES

Bennett, J. M. 1987 Theoretical properties of three-dimensional interactive boundary layers. PhD thesis, University of London.

Bertram, C. D. & Godbole, S. A. 1997 LDA measurements of velocities in a simulated collapsed tube. *Trans. ASME J. Biomech. Engng* **119**, 357–363.

Blyth, M. G. & Mestel, A. J. 1999 Steady flow in a dividing pipe. *J. Fluid Mech.* **401**, 339–364.

Cassot, F., Zagzoule, M. & Marc-Vergnes, J. P. 2000 Hemodynamics role of the circle of Willis in stenoses of internal carotid arteries. an analytical solution of a linear model. *J. Biomech* **33**, 395–405.

Comer, J. K., Kleinstreuer, C. & Zhang, Z. 2001*a* Flow structures and particle deposition patterns in double-bifurcation airway models. Part 1. Air flow fields. *J. Fluid Mech.* **435**, 25–54.

Comer, J. K., Kleinstreuer, C. & Zhang, Z. 2001*b* Flow structures and particle deposition patterns in double-bifurcation airway models. Part 2. Aerosol transport and deposition. *J. Fluid Mech.* **435**, 55–80.

Cummings, L. J., Wattis, S. L. & Graham, J. A. D. 2004 The effect of ureteric stents on urine flow: reflux. *J. Math. Biol.* **49**, 56–82.

Ferrandez, A., David, T., Bamford, J. & Guthrie, A. 2000 Computational models of blood flow in the circle of Willis. *Computer Meth. Biomech. Biomed. Engng* **4**, 1–26.

Gao, E., Young, W. L., Ornstein, E., Pile-Spellman, J. & Ma, Q. 1997 A theoretical model of cerebral hemodynamics: application to the study of arteriovenous malformations. *J. Cerebral Blood Flow Metab.* **17**, 905–918.

Gnanalingham, K., Taylor, W. & Watkin, L. 2002 Dual technique for obliteration of small arteriovenous malformations. *Brit. J. Neurosurg.* **16** (4), 376–380.

Griffiths, D. J. 1971 Hydrodynamics of male micturition – I: theory of steady flow through elastic-walled tubes. *Med. Biol. Engng* **9**, 581–588.

Griffiths, D. J. 1987 Dynamics of the upper urinary tract: I. peristaltic flow through a distensible tube of limited length. *Phys. Med. Biol.* **32**, 813–822.

Griffiths, D. J., Constantinou, C. E., Mortensen, J. & Djurhuus, J. C. 1987 Dynamics of the upper urinary tract: II. the effect of variations or peristaltic frequency and bladder pressure on pyeloureteral pressure/flow relations. *Phys. Med. Biol.* **32**, 823–833.

Grotberg, J. B. & Jensen, O. E. 2004 Biofluidmechanics of flexible tubes. *Annu. Rev. Fluid Mech.* **36**, 121–147.

Hademenos, G. J., Massoud, T. F. & Vinuela, F. 1996 A biomathematical model of intracranial arteriovenous malformations based on electrical network analysis. theory and hemodynamics. *Neurosurgery* **38**, 1005–1015.

Handa, T., Negoro, M., Miyachi, S. & Sugita, K. 1993 Evaluation of pressure changes in feeding arteries during embolization of intracerebral arteriovenous malformations. *J. Neurosurg.* **79**, 383–389.

Hillen, B., Drinkenburg, B. A. H., Hoogstraten, H. W. & Post, L. 1988 Analysis of flow and vascular resistance in a model of the circle of Willis. *J. Biomech.* **21**, 807–814.

Hillen, B., Hoogstraten, H. W. & Post, L. 1986 A mathematical model of the flow in the circle of Willis. *J. Biomech.* **19**, 187–194.

https://doi.org/10.1017/S0022112008003522 Published online by Cambridge University Press

Kufahl, R. H. & Clark, M. E. 1985 A circle of Willis simulation using distensible vessels and pulsatile flow. *J. Biomech. Engng* **107**, 112–122.

Luo, X. Y. & Pedley, T. J. 2000 Multiple solutions and flow limitation in collapsible channel flows. *J. Fluid Mech.* **420**, 301–324.

Marini, B. D. & Smith, C. R. 2002 The influence of impinging boundary layer vorticity packets on turbulent juncture flow behavior. In *Proc. 2nd Intl Sympo. on Turbulence and Shear Flow Phenomena, Stockholm, Sweden* (ed. J. A. Eaton & M. Sommerfield), pp. 245–254. Springer.

Marzo, A., Luo, X. Y. & Bertram, C. D. 2005 Three-dimensional collapse and steady flow in thick-walled flexible tubes. *J. Fluids Struct.* **20**, 817–835.

Mittal, R. & Iaccarino, G. 2005 Immersed boundary methods. *Annu. Rev. Fluid Mech.* **37**, 239–261.

Olufsen, M. S. 1999 Structured tree outflow condition for blood flow in larger systemic arteries. *Am. J. Physiol. Heart Circ. Physiol.* **276**, H257–268.

Ovenden, N. C., Smith, F. T. & Wu, G. X. 2008 The effects of nonsymmetry in a branching flow network. *J. Engng Maths* (to appear).

Pedley, T. J. 1997 Pulmonary fluid dynamics. *Annu. Rev. Fluid Mech.* **9**, 229–274.

Peskin, C. S. 2002 The immersed boundary method. *Acta Numerica* pp. 1–39.

Seal, C. V. & Smith, C. R. 1997 Intertwining laminar necklace vortices. *Phys. Fluids* **9** (9).

Seal, C. V., Smith, C. R., Akin, O. & Rockwell, D. 1995*a* Quantitative characteristics of a laminar, unsteady necklace vortex system in a rectangular block-flat plate juncture. *J. Fluid Mech.* **286**, 117–135.

Seal, C. V., Smith, C. R. & Rockwell, D. 1995*b* Vorticity distribution in endwall junctions. *AIAA Paper* 95-2238.

Smith, F. T. 1977 Steady motion through a branching tube. *Proc. R. Soc. Lond.* A **355**, 167–187.

Smith, F. T. 1978 Flow through symmetrically constricted tubes. *J. Inst. Maths Applics.* **21**, 145–156.

Smith, F. T., Dennis, S. C. R., Jones, M. A., Ovenden, N. C., Purvis, R. & Tadjfar, M. 2003*a* Fluid flow through various branching tubes. *J. Engng Maths* **47**, 277–298.

Smith, F. T. & Gajjar, J. S. B. 1984 Flow past wing-body junctions. *J. Fluid Mech.* **144**, 191–215.

Smith, F. T. & Jones, M. A. 2000 One-to-few and one-to-many branching tube flows. *J. Fluid Mech.* **423**, 1–31.

Smith, F. T, Ovenden, N. C, Franke, P. & Doorly, D. J. 2003*b* What happens to pressure when a flow enters a side branch? *J. Fluid Mech.* **479**, 231–258.

Smith, F. T. & Timoshin, S. N. 1996 Blade-wake interactions and rotary boundary layers. *Proc. R. Soc. Lond.* A **452**, 1301–1329.

Stacey, R. & Kitchen, N. D. 1999 Recent advances in the management of cerebrovascular disease: the diminishing role of the surgeon? *Ann. R. Coll. Surg. Engrs* **81**, 86–89.

Tadjfar, M. & Himeno, R. 2001 Parallel multi-zone multi-block solver to study arterial branches in the human vascular system. In *Proc. Intl Mech. Engng Congr. and Expo-2001, New York*, pp. 1–7. ASME.

Tadjfar, M. & Smith, F. T. 2004 Direct simulations and modelling of basic three-dimensional bifurcating tube flows. *J. Fluid Mech.* **519**, 1–32.

Ursino, M. & Lodi, C. A. 1997 A simple mathematical model of the interaction between intracranial pressure and cerebral hemodynamics. *J. Appl. Physiol.* **82**, 1256–1269.

Wilquem, F. & Degrez, G. 1997 Numerical modelling of steady inspiratory airflow through a three-generation model of the human central airways. *Trans. ASME: J. Biomech. Engng* **119**, 59–67.

Zagzoule, M. & Marc-Vergnes, J. P. 1986 A global mathematical model of the cerebral circulation in man. *J. Biomech.* **19** (12), 1015–1022.

Zhao, Y. & Lieber, B. B. 1994 Steady inspiratory flow in a model symmetric bifurcation. *Trans. ASME: J. Biomech. Engng* **116**, 488–496.

https://doi.org/10.1017/S0022112008003522 Published online by Cambridge University Press